ORIGINAL ARTICLE

Phenolic Acid-Functionalized Gold Nanoparticles: A Theranostic Approach to Radiosensitization and CT Contrast Enhancement in Breast Cancer

Elahe Hajisattari [1], Zeynab Seraj [2], Zahra Amiri [3], Alireza Solhi [1*]

[1] *Department of Radiology, Faculty of Paramedical Sciences, Ardabil University of Medical Sciences, Ardabil, Iran*

[2] *Department of Biomedical Engineering and Medical Physics, Shahid Beheshti University of Medical Sciences, Tehran, Iran*

[3] *Department of Medical Physics, Faculty of Medicine, Mashhad University of Medical Sciences, Mashhad, Iran*

*Corresponding Author: Alireza Solhi

Received: 04 September 2026 / Accepted: 04 October 2026

Email: karassaraaa@gmail.com

Abstract

Purpose: Radiotherapy (RT) resistance and inadequate CT contrast sensitivity limit the efficacy of breast cancer (BC) management. This study introduces a theranostic platform based on gallic acid functionalized gold nanoparticles (Au@GA NPs) for dual radiosensitization and CT contrast enhancement.

Materials and Methods: Au@GA NPs were produced by a green method utilizing GA as both a reducing and capping agent. The physicochemical characteristics were analyzed using UV-Vis, XRD, SEM, and TEM techniques. Cytotoxic effects and radiosensitization were assessed in MCF-7 (malignant) and MCF-10A (non-malignant) cell lines by an MTT assay in conjunction with 6 MV X-ray exposure (4 Gy). The efficacy of CT contrast was evaluated against Omnipaque (iohexol 300) at 80, 120, and 160 kVp. Apoptosis was measured using Annexin V FITC/PI flow cytometry.

Results: Spherical Au@GA NPs (20 nm) exhibited a characteristic SPR peak at 520 nm. Selective cytotoxicity was observed: MCF 7 viability decreased to 68% at 200 µg/mL, while MCF-10A remained >82%. Combination with 4 Gy irradiation reduced MCF 7 viability to 39% (vs. 78% without NPs), demonstrating potent radiosensitization. CT attenuation of Au@GA NPs was up to 2.5 fold higher than Omnipaque at 80 kVp. Flow cytometry revealed that the combined treatment induced 81.9% total non viable cells (53.7% late apoptosis), versus 25.7% for radiation alone.

Conclusion: The Au@GA NP platform offers a dual function strategy, enhancing tumor radiosensitivity while providing superior CT contrast, positioning it as a promising candidate for image guided RT (IGRT) in BC.

Keywords: Gold Nanoparticles; Gallic Acid; Radiosensitization; Computed Tomography; Breast Cancer; Theranostics.

PROOF

Copyright © 2027 Tehran University of Medical Sciences.
This work is licensed under a Creative Commons Attribution-NonCommercial 4.0 International license (https://creativecommons.org/licenses/by-nc/4.0/). Noncommercial uses of the work are permitted, provided the original work is properly cited.
DOI:

1. Introduction

Breast cancer (BC) continues to be the most often identified disease and the primary cause of cancer-related deaths among women worldwide, with almost 2.3 million new diagnoses and more than 685,000 fatalities per year [1]. Notwithstanding significant progress in early diagnosis and many treatment approaches, BC remains a formidable clinical obstacle, especially because of its genetic diversity, tendency to metastasize, and the emergence of treatment resistance [2]. Radiotherapy (RT) is a fundamental approach in the treatment of BC, yet its clinical effectiveness is often hindered by inherent or developed tumor radioresistance and toxicity that restricts doses to surrounding healthy tissues such as the heart, lungs, and skin [3]. These limitations underscore the urgent need for novel approaches that specifically increase tumor radiosensitivity while preserving healthy tissues [4]. Concurrently, computed tomography (CT) has emerged as an indispensable modality for BC staging and treatment planning, yet conventional iodine-based contrast agents (CAs) lack the sensitivity required for early tumor detection and molecular characterization [5]. The convergence of these challenges has motivated the exploration of multifunctional nanoplatforms capable of addressing both therapeutic and diagnostic requirements within a single integrated system [6, 7].

Gold nanoparticles (Au NPs) have garnered considerable attention in this domain, primarily because of their distinctive physicochemical characteristics, such as a high atomic number (Z = 79), pronounced photoelectric absorption, ease of surface modification, and favorable biocompatibility [8, 9]. As reviewed by Mauro *et al.* (2021), AuNPs exhibit surface plasmon resonance properties that render them suitable for both imaging (CT, photoacoustic) [10] and therapeutic (photothermal, radiosensitization) applications [11, 12]. Siddique and Chow further emphasized that the high atomic number of Au endows AuNPs with dual functionality: potent radiosensitization through photoelectric and Auger electron interactions, and superior CT contrast enhancement compared to iodine-based agents [13]. These intrinsic properties position AuNPs as ideal platforms for theranostic applications, simultaneously enabling image-guided RT and treatment response monitoring [14]. Recent advances have demonstrated that surface functionalization of AuNPs with bioactive molecules can further augment their therapeutic and diagnostic potential [15]. Phenolic acids, a class of naturally occurring polyphenolic compounds widely distributed in plants, have drawn substantial interest owing to their inherent antioxidant, anti-inflammatory, and anticancer properties [16]. Gallic acid (3,4,5-trihydroxybenzoic acid, GA), as a typical phenolic acid, demonstrates pronounced pro-apoptotic and anti-proliferative activities via mechanisms that include reactive oxygen species production, mitochondrial impairment, and regulation of critical signaling cascades [17]. Importantly, phenolic acids serve as both reducing and capping agents in the green synthesis of AuNPs, offering an eco-friendly, biocompatible alternative to conventional chemical methods [18]. Tarantino *et al.* (2025) demonstrated that polyphenol-coated AuNPs synthesized using Laurus nobilis leaf extract significantly enhanced RT efficacy in MCF 7 BC cells at lower radiation doses [19]. Similarly, López-Valverde (2024) established that AuNP concentrations provide both diagnostic contrast in CT and therapeutic dose enhancement under clinical conditions, achieving dose enhancement and radiosensitization in superficial tumors [20]. These findings support the rationale that functionalization of AuNPs with phenolic acids creates a synergistic platform wherein the inherent bioactivity of the phenolic compound complements the physicochemical properties of the nanoparticle core, potentially enhancing cellular uptake, tumor targeting, and therapeutic efficacy [21].

Notwithstanding the distinct promise of AuNPs as radiosensitizers and CT CAs, as well as the documented bioactivity of phenolic compounds, the integration of these functionalities into a unified phenolic acid-functionalized AuNP platform for combined radiosensitization and CT imaging in BC remains relatively underexplored. The present study addresses this gap by developing a green-synthesized GA-functionalized Au NP platform and thoroughly evaluating its dual theranostic capabilities. The central hypothesis is that these NPs will function as an effective dual-modality theranostic platform [22], simultaneously enhancing radiation-induced cytotoxicity in MCF 7 BC cells through radiosensitization while providing superior CT

PROOF

contrast enhancement compared to conventional iodine-based agents.

2. Materials and Methods

2.1. Materials

Sigma-Aldrich (USA) served as the supplier for Tetrachloroauric(III) acid trihydrate ($HAuCl_4 \cdot 3H_2O$, 99.9%), gallic acid ($C_7H_6O_5$), MTT (3-(4,5-dimethylthiazol-2-yl)-2,5-diphenyltetrazolium bromide), DAPI (4′,6-diamidino-2-phenylindole), Triton X-100, dimethyl sulfoxide, and trypan blue stain. Gibco (UK) was the source of Dulbecco's Modified Eagle Medium, fetal bovine serum, and trypsin-EDTA. GE Healthcare provided Iohexol 300. The rest of the chemicals and reagents met analytical grade specifications and were utilized directly, with no further purification steps. Deionized water was employed throughout the entire study. The MCF 7 human breast adenocarcinoma cell line was sourced from the National Cell Bank of Iran (Pasteur Institute, Tehran, Iran).

2.2. Synthesis of Au@GA NPs

Au@GA NPs were prepared through a single-step green synthesis approach, with GA acting as both the reducing and stabilizing agent. In a typical procedure, 0.5 mL of a 10 mM GA solution (pH = 10) was introduced dropwise into 10 mL of 0.6 mM $HAuCl_4 \cdot 3H_2O$ (pH = 10) while undergoing continuous magnetic stirring. A 2 mM NaOH solution was used to adjust the pH and maintain optimal reaction conditions. The reaction mixture was then stirred vigorously at room temperature for 30 minutes, during which a stable wine-red coloration developed, signaling the successful formation of Au NPs. After synthesis, the NPs were purified to eliminate unreacted precursors and by-products. To remove unbound GA and residual Au ions, the product was subjected to three successive centrifugation cycles at 12,000 rpm for 15 minutes each, followed by decanting the supernatant and resuspending the pellet in deionized water. The purified NPs were kept at 4°C for subsequent characterization and experiments [23].

2.3. Characterization of Au@GA NPs

The synthesized Au@GA NPs were characterized for their physicochemical properties by employing several complementary analytical techniques. UV-Vis absorption spectroscopy was carried out on a SPEKOL 2000 double-beam spectrophotometer across the 400–700 nm wavelength range to verify successful synthesis and assess colloidal stability [19]. Crystalline structure and phase purity were evaluated through X-ray diffraction (XRD) on a PANalytical X'Pert Pro diffractometer equipped with Cu-Kα radiation (λ = 1.5406 Å), scanning a 2θ range of 20°–90°, with the resulting diffraction peaks matched against the standard JCPDS database for metallic Au. Surface morphology was examined using a MIRA3 TESCAN field emission SEM operated at 15 kV. In addition, the morphology, size, and shape of the NPs were further explored by TEM on a Zeiss EM10C microscope operated at 100 kV. Particle size analysis was conducted on a minimum of 100 NPs using Digital Micrograph software to establish the average diameter and size distribution.

2.4. Cell Culture

MCF 7 human breast adenocarcinoma cells and MCF-10A normal breast epithelial cells were maintained in 25-cm² tissue culture flasks at 37°C within a humidified environment supplemented with 5% CO_2. For MCF 7 cells, DMEM enriched with 10% FBS, 100 U/mL penicillin, and 100 µg/mL streptomycin was used. MCF-10A cells were grown in DMEM medium containing 5% horse serum, 20 ng/mL EGF, 0.5 µg/mL hydrocortisone, 10 µg/mL insulin, and 1% penicillin. Once cultures approached roughly 80% confluency, cells were detached using 0.25% trypsin-EDTA, kept at 37°C for 3–5 minutes, and then centrifuged at 1200 rpm for 5 minutes. The supernatant was removed, and the resulting cell pellet was resuspended in fresh culture medium before subculturing or seeding for experiments [10].

2.5. Cytotoxicity Assessment

Cell viability was determined through the MTT assay performed in biological triplicate (n = 3 independent experiments), with 6 technical replicates per concentration. To examine the cytotoxic effects of Au@GA NPs, MCF 7 and MCF-10A cells were plated

PROOF

into 96-well plates at 5 × 10^3 cells per well and kept at 37°C under a 5% CO_2 humidified atmosphere for 24 hours. The cells were subsequently exposed to various concentrations of Au@GA NPs (0, 6.25, 12.5, 25, 50, 100, 150, and 200 µg/mL) and incubated for 24 hours. After treatment, the culture medium was aspirated, and 100 µL of MTT solution (0.5 mg/mL) was added to each well, followed by a 4-hour incubation at 37°C. The formazan crystals that formed were then solubilized in 100 µL of DMSO, and absorbance was recorded at 570 nm using an ELISA microplate reader [24].

2.6. CT Contrast Enhancement Evaluation

The X-ray attenuation performance of the synthesized Au@GA NPs was assessed in comparison with Omnipaque (iohexol 300), an iodine-based contrast agent routinely applied in clinical practice. A set of solutions was prepared, consisting of Au@GA NPs at concentrations between 0.5 and 10 mM Au, along with iohexol 300 at matching iodine concentrations. These solutions were dispensed into 0.5 mL Eppendorf tubes, which were subsequently mounted inside a phantom for imaging. Image acquisition was conducted on a 16-slice clinical system (GE Healthcare) employing the following parameters: tube potentials of 80, 120, and 160 kVp; a tube current of 250 mA; an exposure time of 1000 ms; a slice thickness of 0.625 mm; a scan field of view of 250 × 250 mm; a display FOV of 130 × 130 mm; and a pitch of 1. After capturing the images of the samples, a uniform region of interest was defined on each image. X-ray attenuation, expressed in Hounsfield units (HU), was then quantified for both Au@GA NPs and iohexol 300 through analysis of the region of interest on the images. This step was repeated across all samples to enable comparison of their X-ray attenuation behavior at the various tube potentials and concentrations [25].

2.7. Radiation Dose Enhancement Evaluation

The radiosensitizing potential of Au@GA NPs was investigated by delivering X-ray irradiation to MCF 7 and MCF-10A cells. A 6 MV beam produced by an Elekta Compact linear accelerator (Elekta AB, Stockholm, Sweden) was used to administer a 4 Gy dose. The beam was delivered at a dose rate of 1.717 cGy per monitor unit, with a source-to-surface distance of 100 cm and a field size of 12 × 16 cm^2. The choice of a single 4 Gy fraction was based on its clinical relevance as a per-fraction dose in BC RT, as well as its capacity to induce measurable DNA damage appropriate for assessing radiosensitization in vitro. Before irradiation, cells were exposed to Au@GA NPs at 6.25, 12.5, 25, 50, 100, and 150 µg/mL for 24 hours. After irradiation, an additional 24-hour incubation at 37°C in a 5% CO_2 humidified atmosphere was carried out prior to downstream analyses. To promote uniform dose distribution and limit backscatter radiation, 1 cm Perspex plates were arranged above and below the cell culture plates, and a further 1 cm solid water phantom was placed beneath the samples [26].

2.8. Flow Cytometric Analysis of Apoptosis

Apoptosis was assessed by Annexin V-FITC/PI double staining coupled with flow cytometry. MCF 7 cells in the logarithmic growth phase were plated into 6-well plates at 2 × 10^5 cells per well. Four treatment groups were established: control, Au@GA NPs alone (100 µg/mL), radiation alone (4 Gy), and Au@GA NPs (100 µg/mL) combined with radiation. After a 24-hour treatment with Au@GA NPs (100 µg/mL), the irradiation groups received 4 Gy X-ray, followed by a further 24-hour incubation at 37°C in a 5% CO_2 humidified atmosphere before apoptosis analysis. Cells were then harvested with 0.25% trypsin-EDTA, rinsed with phosphate-buffered saline, and resuspended in 100 µL of binding buffer. Annexin V-FITC (5 µL) and propidium iodide (40 µg/mL) were introduced to the cell suspension, and the samples were kept in the dark at room temperature for 15 minutes. Apoptosis was evaluated on a BD FACS Calibur flow cytometer (BD Biosciences, CA, USA). Populations corresponding to early apoptotic (Annexin V^+/PI^-), late apoptotic (Annexin V^+/PI^+), necrotic (Annexin V^-/PI^+), and viable (Annexin V^-/PI^-) cells were analyzed using FlowJo™ software version 7 (BD Life Sciences, USA) [22].

2.9. Statistical Analysis

Viability data were obtained from three independent biological replicates with six technical replicates per condition. Results are presented as mean ± SD. Statistical significance was assessed by one-way ANOVA with Tukey's post-hoc test for multiple

PROOF

comparisons, or by Student's t-test for pairwise comparisons, using GraphPad Prism 10.4.0. Significance thresholds were set at *p < 0.05, **p < 0.01, and ***p < 0.001.

3. Results

3.1. Synthesis and characterization of Au@GA NPs

Successful formation of Au@GA NPs was verified through UV-Visible absorption spectroscopy. The UV-Vis spectrum of Au@GA NPs, presented in Fig. 1a, displayed a distinctive SPR band centered at 520 nm, while uncoated Au NPs exhibited their plasmon peak at 535 nm. This blue shift from 535 nm to 520 nm following GA functionalization provided confirmation of effective surface modification. Moreover, the development of a stable wine-red coloration during synthesis served as an additional indicator of Au^{3+} reduction to metallic Au NPs.

XRD analysis was employed to investigate the crystalline structure and phase purity of the synthesized Au@GA NPs. The XRD pattern, shown in Fig. 1b, exhibited five well-defined diffraction peaks at 2θ values of approximately 38.2°, 44.4°, 64.6°, 77.6°, and 81.8°, which correspond to the (111), (200), (220), (311), and (222) crystallographic planes of the face-centered cubic structure of metallic Au, respectively (JCPDS No. 04-0784). The prominent (111) diffraction peak reflects the preferential orientation and high crystallinity of the NPs. The absence of any additional impurity peaks confirmed the phase purity of the synthesized nanomaterials.

Surface morphology of the synthesized NPs was investigated by SEM. The SEM micrograph (Fig. 1c) revealed spherical NPs with relatively uniform morphology and favorable dispersion, reflecting the effective colloidal stability conferred by the GA coating. TEM analysis was carried out to further examine the morphology, size, and size distribution of the NPs (Fig. 1d). TEM micrographs confirmed the spherical shape of the NPs. Particle size analysis, performed on a minimum of 100 NPs using ImageJ software, yielded an average particle size of approximately 20 nm with a narrow size distribution. The mean particle size of approximately 20 nm reported in this study represents the metallic core diameter determined by TEM. Hydrodynamic diameter and polydispersity index (PDI), which would more fully capture the contribution of the GA shell and hydration layer in dispersion, were not measured and should be included in future physicochemical characterization.

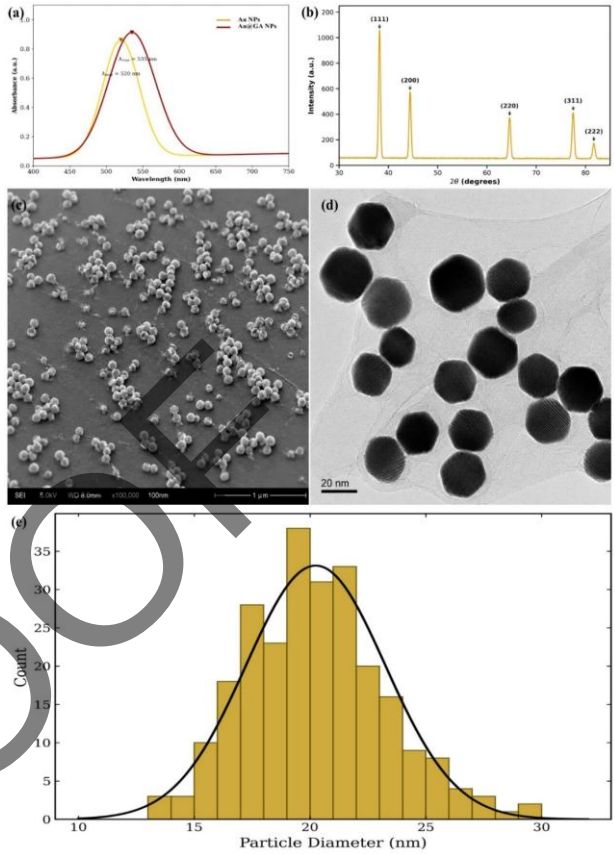


Figure 1. Physicochemical characterization of Au@GA NPs. (a) UV-Vis spectra of Au NPs and Au@GA NPs; (b) XRD pattern confirming fcc structure of metallic gold; (c) SEM image showing spherical morphology; (d) TEM image confirming spherical morphology, (e) Particle size distribution histogram of Au@GA NPs derived from TEM analysis

3.2. Au@GA NPs Induce Selective Cytotoxicity in BC Cells

To evaluate the biocompatibility and anticancer potential of the synthesised Au@GA NPs, their cytotoxic effects were assessed on both non-tumorigenic (MCF-10A) and cancerous (MCF-7) breast epithelial cell lines using the MTT assay across a concentration range of 6.25–200 µg/mL (Figure 2).

As presented in Figure 2, exposure of MCF-10A cells to increasing concentrations of Au@GA NPs (6.25, 12.5, 25, 50, 100, 150, and 200 µg/mL) resulted in cell viabilities of 97%, 95%, 93%, 90%, 87%, 83%,

PROOF

and 82%, respectively, compared to 100% viability in untreated controls. Under identical treatment conditions, MCF-7 cells exhibited markedly lower viabilities of 94%, 87%, 81%, 78%, 75%, 73%, and 68%, respectively.

Quantitative analysis revealed that increasing the

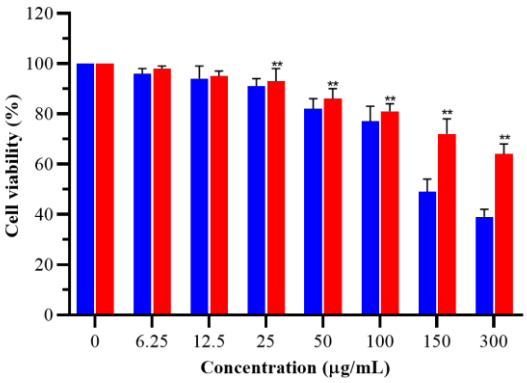


Figure 2. Cell viability results of different concentrations of Au@GA NPs on both MCF-7 and MCF-10A cell lines. Gold nanoparticles (Au NPs)

nanoparticle concentration from 6.25 to 200 μg/mL reduced cell viability in MCF-10A cells from 97.83% to 83.05%, corresponding to an approximate 14% reduction ($p > 0.05$). In contrast, MCF-7 cells showed a more pronounced decline from 93.00% to 67.94% under the same concentration range, representing a ~26% decrease ($p > 0.05$). These findings demonstrate that MCF-7 cancer cells are significantly more susceptible to Au@GA NP treatment than their healthy MCF-10A counterparts, with the differential sensitivity being consistently observed across all tested concentrations.

This selective cytotoxicity likely arises from fundamental biological differences between malignant and normal cells, including altered membrane permeability, enhanced endocytic activity, elevated metabolic rates, and distinct redox environments characteristic of cancer cells. The observed preferential toxicity towards cancerous cells underscores the potential of Au@GA NPs for targeted anticancer applications with minimized off-target effects on healthy tissues.

Our results are in good agreement with previously reported findings. Rozalen *et al.* investigated the cytotoxic profile of Ag NPs in MDA-MB-231 and MCF-7 BC cells alongside normal MCF-10A breast epithelial cells. Their apoptosis analysis revealed negligible apoptotic induction in MCF-10A cells, whereas MDA-MB-231 and MCF-7 cells exhibited pronounced apoptotic body formation, particularly at Ag NP concentrations exceeding the determined IC_{50} values [28]. This concordance further supports the selective anticancer activity of Au@GA NPs and highlights their translational promise as a biocompatible nanoplatform.

3.3. Radiosensitization Effects of Au@GA NPs

To evaluate the radiosensitizing potential of Au@GA NPs, the viability of MCF-7 (BC) and MCF-10A (normal breast epithelial) cells was assessed following combined treatment with varying concentrations of Au@GA NPs and 4 Gy X-ray irradiation (6 MV), as illustrated in Figure 3.

Figure 3 presents the cell viability profiles of both cell lines exposed to increasing concentrations of Au@GA NPs (0–150 μg/mL) under 4 Gy irradiation. For MCF-10A cells, viabilities declined progressively from 88% (0 μg/mL) to 84%, 81%, 77%, 71%, 69%, and 66% at concentrations of 6.25, 12.5, 25, 50, 100, and 150 μg/mL, respectively. In contrast, MCF-7 cells exhibited substantially lower viabilities of 78%, 69%, 63%, 56%, 50%, 44%, and 39% under identical irradiation and concentration conditions.

Notably, in the absence of irradiation, baseline cell viabilities for MCF-10A and MCF-7 were 88% and 78%, respectively (at 0 μg/mL Au@GA NPs). Upon exposure to 4 Gy radiation, cell viabilities decreased further to 66% for MCF-10A and 39% for MCF-7, representing radiation-induced viability reductions of 22% and 39%, respectively. This differential response highlights the significantly greater radiosensitivity of MCF-7 cancer cells compared to normal MCF-10A cells when treated with Au@GA NPs.

These findings demonstrate that Au@GA NPs act as effective radiosensitizers, potentiating the cytotoxic effects of ionizing radiation in a dose-dependent manner. The enhanced radiosensitivity observed in cancer cells can be attributed to the high atomic number ($Z = 79$) of Au, which amplifies local radiation dose deposition through photoelectric and Auger electron interactions, thereby increasing DNA damage and subsequent cell death. The selective radiosensitization of malignant cells over normal cells further underscores the therapeutic potential of this

PROOF

nano-platform for image-guided RT with reduced off-target toxicity.

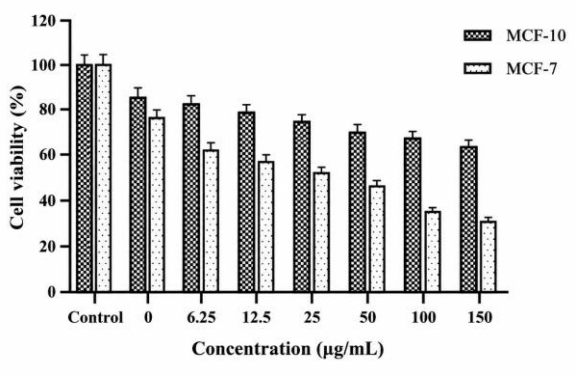


Figure 3. Radiosensitizing effect of Au@GA NPs on MCF-7 and MCF-10A cells following 4 Gy X-ray irradiation. Cell viability was assessed after 24 h of treatment with varying concentrations of Au@GA NPs (0–150 µg/mL) in combination with 4 Gy irradiation. Data are presented as mean ± SD (n = 3 independent experiments). Au@GA NPs: gallic acid-functionalized gold nanoparticles

3.4. X-Ray Attenuation Properties of Au@GA NPs Versus Omnipaque

The X-ray attenuation characteristics of the synthesized Au@GA NPs were systematically evaluated and compared with Omnipaque (iohexol 300), a clinically employed iodine-based contrast agent. The assessment was performed across a range of molar concentrations of the contrast elements (Au vs. iodine) and at three clinically relevant tube potentials: 80, 120, and 160 kVp.

As depicted in Figure 4, CT phantom images of aqueous suspensions demonstrated a concentration-dependent increase in image brightness for both CAs, with higher concentrations yielding greater radiopacity. However, qualitative visual inspection revealed that Au@GA NPs produced notably brighter CT signals compared to Omnipaque at equivalent molar concentrations across all energy levels.

Quantitative analysis of X-ray attenuation, expressed in HU, is presented in Figure 4b. At all tested tube potentials (80, 120, and 160 kVp), the attenuation coefficients of Au@GA NPs were consistently and significantly higher than those of Omnipaque across the entire concentration range (0.5–10 mM). This superior attenuation performance can be attributed to the higher atomic number of Au (Z = 79) compared to iodine (Z = 53), which results in enhanced photoelectric absorption and a greater X-ray scattering cross-section within the diagnostic energy spectrum.

Furthermore, the attenuation efficiency of Au@GA NPs was particularly pronounced at lower tube potentials (80 kVp), where the photoelectric effect predominates, and Au's K-edge (80.7 keV) lies optimally within the energy range. At higher potentials (120 and 160 kVp), although the relative difference diminished slightly, Au@GA NPs still maintained superior contrast enhancement compared to the iodine-based agent.

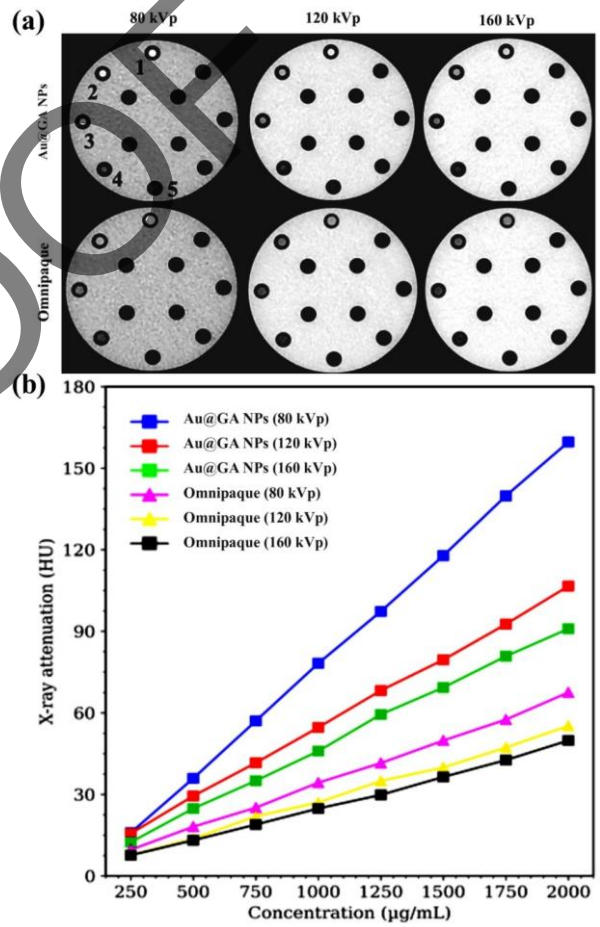


Figure 4. X-ray attenuation properties of Au@GA NPs compared to Omnipaque (iohexol 300). (A) CT phantom images of aqueous suspensions at varying molar concentrations of gold (Au@GA NPs) and iodine (Omnipaque) acquired at 80, 120, and 160 kVp. (B) Quantitative attenuation values (Hounsfield Units, HU) as a function of contrast element concentration at three tube potentials. Data are presented as mean ± SD (n = 3 independent measurements). Au@GA NPs: gallic acid-functionalized gold nanoparticles

PROOF

These findings collectively demonstrate that Au@GA NPs possess superior X-ray attenuation properties compared to conventional iodine-based contrast media, establishing their potential as a more effective CT contrast agent for enhanced tumor visualization and image-guided RT applications.

3.5. Au@GA NPs Enhance Radiation-Induced Apoptosis in MCF-7 BC Cells

Because Au@GA NPs display potential radiosensitization properties in MCF-7 cells, the effect of Au@GA NPs on apoptotic (early + late) cell death following ionizing radiation was explored further. Cells received the IC_{10} concentration of Au@GA NPs for 24 h before being irradiated. Annexin V-FITC/PI double staining combined with flow cytometry was used to separate live cells (Q4, Annexin V^-/PI^-), early apoptotic cells (Q3, Annexin V^+/PI^-), late apoptotic cells (Q2, Annexin V^+/PI^+), and necrotic cells (Q1, Annexin V^-/PI^+). For clarity, the apoptotic cell percentage is defined as the sum of early and late apoptotic cells (Q2 + Q3) among all analyzed cells. As shown in Figure 5a, exposure to Au@GA NPs alone caused a modest rise in the apoptotic population relative to untreated controls. After 4 Gy X-ray irradiation, apoptotic death increased considerably, reaching its highest level in the Au@GA NPs + radiation group (Figure 5b). Quantitative assessment showed that combining Au@GA NPs with 4 Gy irradiation markedly raised both early and late apoptotic populations relative to Au@GA NPs alone or radiation alone. Specifically, the combined treatment produced the greatest proportion of total non-viable (early + late + necrotic) cells (81.86%), compared with Au@GA NPs alone (18.88%),

PROOF

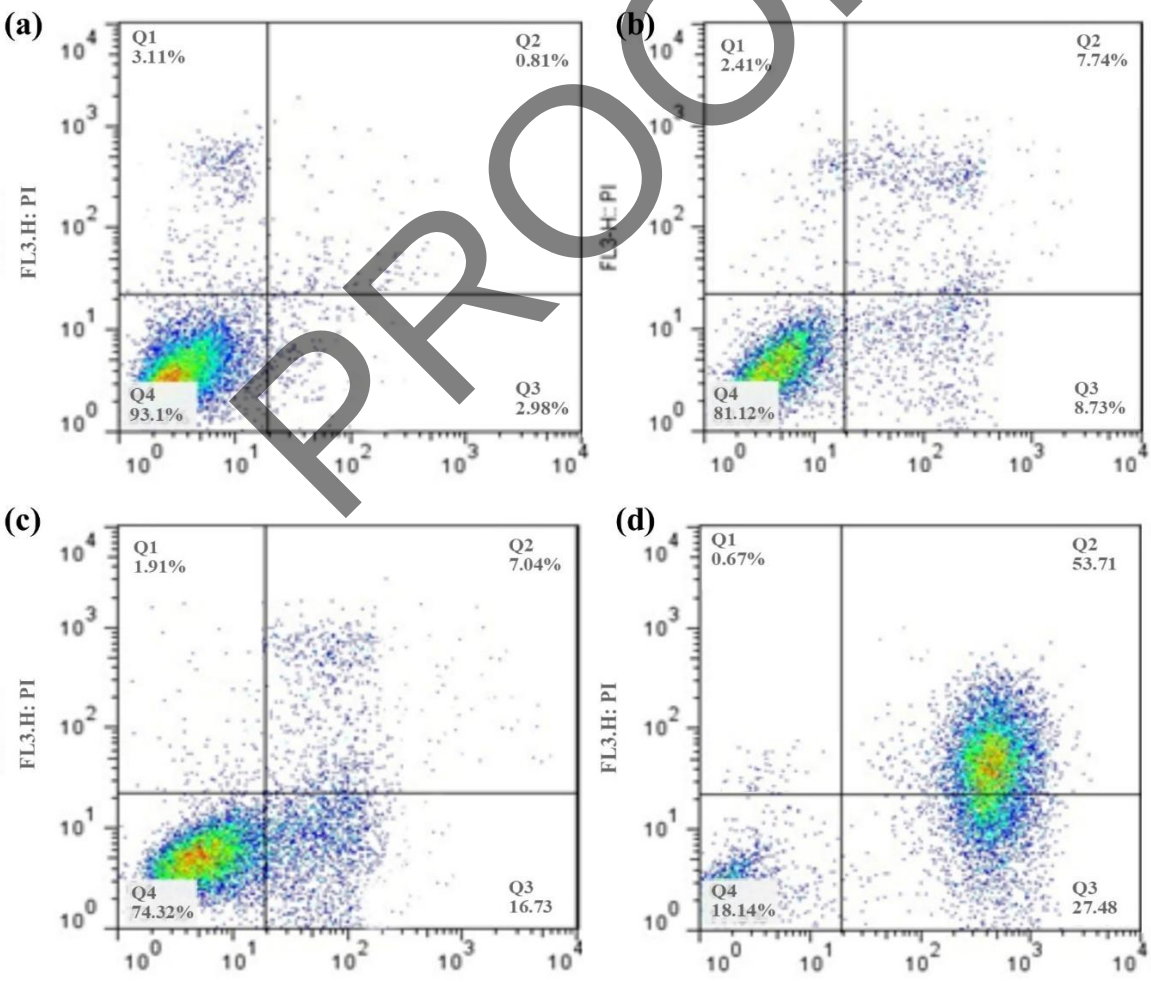


Figure 5. Flow cytometric analysis of apoptosis in MCF-7 cells treated with Au@GA NPs (100 µg/mL) and/or 6 MV (4 Gy) X-ray irradiation using Annexin V-FITC/PI staining. **(a)** Representative dot plots showing live (Q4), early apoptotic (Q3), late apoptotic (Q2), and necrotic (Q1) cell populations in untreated controls; **(b)** Au@GA NPs alone; **(c)** radiation alone (4 Gy); and **(d)** Au@GA NPs + radiation combination

radiation alone (25.68%), and untreated controls (6.90%). Within this group, early apoptosis represented 27.48% and late apoptosis 53.71%, indicating a pronounced shift toward late-stage apoptotic death. By contrast, radiation alone mainly triggered early apoptosis (16.73%) with a smaller late apoptotic fraction (7.04%), whereas Au@GA NPs alone led to 8.73% early and 7.74% late apoptosis (Table 1). Necrosis stayed negligible across all groups, peaking in the control group (3.11%), which suggests that the cell death observed was predominantly apoptotic rather than necrotic. Taken together, these results indicate that Au@GA NPs efficiently sensitize MCF-7 BC cells to radiation-induced apoptosis, with the combined treatment yielding a synergistic increase in apoptotic cell death relative to either modality alone.

4. Discussion

4.1. Main Findings

In the present study, a green-synthesized gallic acid-functionalized Au nanoparticle platform (Au@GA NPs) was successfully developed and systematically characterized for its dual theranostic potential in BC management. The NPs exhibited a spherical morphology with an average diameter of ~20 nm, high crystallinity, and excellent colloidal stability, as confirmed by UV-Vis, XRD, SEM, and TEM analyses. Cytotoxicity assays demonstrated concentration-dependent and selective toxicity towards MCF-7 BC cells (viability reduced to 68% at 200 µg/mL) compared to normal MCF-10A epithelial cells (>82% viability), indicative of the intrinsic anticancer activity of GA and enhanced endocytic uptake in malignant cells. Furthermore, Au@GA NPs acted as potent radiosensitizers, reducing MCF-7 cell viability from 78% (radiation alone) to 39% when combined with 4 Gy X-ray irradiation, an absolute enhancement of approximately 50%, while normal cells exhibited substantially lower sensitivity. CT contrast evaluation revealed superior X-ray attenuation properties compared to the clinical agent Omnipaque, with up to 2.5-fold higher Hounsfield Unit values at 80 kVp, attributable to Au's high atomic number (Z=79) and optimal K-edge energy positioning. Flow cytometric analysis confirmed that the combination treatment synergistically induced apoptotic cell death (81.9% total non-viable cells, comprising 53.7% late and 27.5% early apoptosis) compared to radiation alone (25.7%) or NPs alone (18.9%), with negligible necrosis across all groups. Collectively, these findings establish Au@GA NPs as an effective dual-modality theranostic platform that simultaneously enhances radiation-induced cytotoxicity through physical (photoelectric/Auger) and biological (ROS-mediated) mechanisms while providing superior CT contrast enhancement, thereby positioning this biocompatible nanoplatform as a promising candidate for image-guided RT and personalized BC treatment [27, 28].

4.2. Au NPs as CT CAs

Au NPs exhibit superior X-ray attenuation due to their high atomic number (Z=79), making them promising alternatives to conventional iodine-based CAs for CT imaging. This property enables enhanced tumor visualization and precise margin detection.

MJ Hernández-Esparza, *et al.* [29] developed a hybrid nanoplatform consisting of AuNPs, 3MPS, and

PROOF

Table 1. Quantitative analysis of cell death in MCF-7 cells treated with Au@GA NPs, with and without 4 Gy X-ray irradiation, based on Annexin V-FITC/PI flow cytometric analysis. Values represent the percentage of necrotic (Q1), early apoptotic (Q3), late apoptotic (Q2), and total non-viable (Q1 + Q2 + Q3) cells after 24 h of treatment

Treatment	Live Cells (Q4)	Necrosis (Q1)	Late Apoptosis (Q2)	Early Apoptosis (Q3)	Total Non-Viable (Q1+Q2+Q3)
Control	93.10	3.11	0.81	2.98	6.90
Au@GA NPs	81.12	2.41	7.74	8.73	18.88
Radiation	74.32	1.91	7.04	16.73	25.68
Au@GA NPs + Radiation	18.14	0.67	53.71	27.48	81.86

methotrexate (MTX) for cancer treatment. The NPs (5 nm) with 3MPS as a stabilizing agent achieved 80 ± 5% drug loading efficiency, with 80% MTX released within 1 hour and 95% within 24 hours. The nanosystem induced concentration-dependent cytotoxicity and apoptosis through ROS generation in B16-F10 and HeLa cells. The Au core provides inherent CT contrast capability for future theranostic applications.

Moreover, M Rozalen, *et al.* [30] synthesized silver NPs conjugated with MTX (AgNPs-MTX) for colon and lung cancer treatment. The spherical NPs had HRTEM sizes of 11.13 nm (AgNPs) and 15.2 nm (AgNPs-MTX400), with 40.4% w/w drug loading. The system exhibited sustained release (77-85% within 24 hours) following Higuchi diffusion-controlled kinetics. AgNPs-MTX400 reduced IC50 to 23 µg/mL in HTC-116 cells, demonstrating enhanced anticancer activity with reduced systemic toxicity in zebrafish models. The high atomic number of metals provides inherent CT contrast potential. In another study, Priyanka Murawala, *et al.* [31] developed BSA-capped AuNPs (Au-BSA) for MTX delivery to MCF-7 cells. BSA acted as both a reducing and capping agent. Zeta potential shifted from −28.9 to −13.9 mV and SPR from 527 to 540 nm after MTX loading, confirming successful drug loading. Release was higher at pH 4 than at pH 7.4, consistent with lysosomal release. Au-BSA-MTX induced ~20% greater cell killing than free MTX through apoptosis, with increased uptake, Ki-67 reduction, DNA fragmentation, and Caspase-3 activation. The Au core provides inherent CT contrast for future theranostic applications.

4.3. Au NPs as Radiosensitizers in RT

Au NPs enhance RT efficacy through physical mechanisms (photoelectric effect, secondary electron production) and biological effects (ROS generation, DNA damage) [32]. Radiosensitization efficiency depends critically on particle size, cellular uptake, and surface functionalization [33]. Also, Devika B Chithrani, *et al.* [34] systematically evaluated the effect of AuNP size (14, 50, and 74 nm) on radiosensitization under photon energies of 105 kVp, 220 kVp, and 6 MVp. The 50 nm AuNPs exhibited the highest cellular uptake and produced the greatest radiosensitization enhancement factor (REF = 1.43 at 220 kVp), compared to 14 nm (REF = 1.20) and 74 nm (REF = 1.26). At 105 kVp, the 50 nm particles achieved an REF of 1.66, and at 6 MVp, REF was 1.17. Immunofluorescence staining for γ-H2AX and 53BP1 foci confirmed a significant increase in DNA double-strand breaks in AuNP-treated cells. The authors concluded that 50 nm spherical AuNPs maximize cellular internalization and provide the strongest radiosensitization across both kilovoltage and megavoltage energy spectra. Furthermore, Somayeh Sadat Mehrnia, *et al.* [35] conjugated 10 nm AuNPs with AS1411 aptamer to target nucleolin-overexpressing BC cells. Characterization confirmed conjugation via an SPR shift from 518 to 525 nm and a hydrodynamic size increase from 18.6 to 25 nm, with an aptamer: NP ratio of 72.16 ± 4.7. The sensitization enhancement ratio (SER) for AS1411/GNPs was 1.35 for MCF-7, 1.66 for MDA-MB-231, and 1.91 for mammospheres under 4 MeV electron beam irradiation, compared to non-targeted GNPs (SER = 1.04 for mammospheres). Flow cytometry and ICP-OES confirmed that AS1411 conjugation significantly increased cellular Au uptake and accumulation, particularly in cancer stem-like cells. In another study, Fatemeh Ghahremani, *et al.* [36] synthesized ultra-small Au nanoclusters (GNCs, 7.7 nm) coated with BSA and functionalized with the AS1411 aptamer. ICP-OES analysis revealed that Apt-GNCs accumulated at 15.33 µg Au/g tumor tissue versus 8.53 µg/g for non-targeted GNCs in 4T1 tumor-bearing mice. In vivo, combination of Apt-GNCs with megavoltage radiation therapy reduced average tumor volume by approximately 39% and extended survival by 9 days. The dose enhancement factor (DEF) was 2.7 for Apt-GNCs compared to 1.3 for non-targeted GNCs. Combination of 2 and 4 Gy radiation with GNCs produced effects comparable to 6 Gy radiation alone. The authors concluded that AS1411-targeted Au nanoclusters serve as efficient, biocompatible, and specific radiosensitizers that significantly enhance megavoltage RT efficacy in nucleolin-overexpressing tumors [37].

4.4. Dual-Modal Applications of Au NPs

Several studies have engineered Au NPs to simultaneously provide diagnostic capabilities (CT imaging) and therapeutic functions (RT, photothermal therapy (PTT), or chemotherapy), enabling real-time

PROOF

treatment monitoring and enhanced therapeutic efficacy [38].

Mohammadreza Ghaffarlou, *et al.* [39] demonstrated the most comprehensive dual-modal application by combining CT imaging capability (via Au's high X-ray attenuation) with radiosensitization and PTT in a single platform. The NPs exhibited excellent photothermal conversion under 808 nm NIR irradiation (temperature increase to ~45°C) and maintained photothermal stability over three cycles. In 4T1 cancer cells, combination of NPs with X-ray and NIR irradiation significantly increased ROS production and decreased cell survival to approximately 35%. In Balb/c mouse models, the triple combination achieved the greatest tumor growth inhibition without noticeable damage to major organs. This system functions as both a radiosensitizer and a photothermal agent, with inherent CT contrast capability enabling imaging-guided therapy. Moreover, Sepideh Hassibian, *et al.* [40] developed Apt-CCM-HG@MTX with dual functionality for colorectal cancer treatment. The hollow Au NPs (51.33 ± 5.70 nm) provided photothermal conversion capability under NIR irradiation, while the AS1411 aptamer enabled active targeting of nucleolin-overexpressing cancer cells. The targeted formulation induced approximately 45% cell death in C26 cells in vitro. In vivo results confirmed that the combination of homologous cell membrane coatings and AS1411 aptamer specificity significantly enhanced tumor accumulation and photothermal effects. The system's design provides inherent potential for CT imaging applications due to Au's high X-ray attenuation coefficient. In addition, Cheng-Hung Li, *et al.* [41] established a dual-modal imaging platform combining CT imaging with fluorescence-guided surgery. The AS1411-DA-AuNPs nanoprobe provided 106% CT contrast enhancement in tumors within 30 minutes, enabling precise tumor localization. Simultaneously, the orange-red fluorescence at 620 nm allowed fluorescence-guided tumor resection, with IVIS imaging confirming 172% higher tumor fluorescence compared to non-targeted controls. While this study focused primarily on imaging, the presence of Au NPs inherently provides radiosensitization potential for future theranostic applications [38].

Sahar Taghavi, *et al.* [42] developed a biomimetic theranostic platform combining CT imaging with targeted chemotherapy. The hollow Au NPs loaded with doxorubicin and decorated with MUC-1 aptamer provided enhanced CT radiological contrast in tumor tissues, enabling simultaneous therapy monitoring and tumor imaging. The system exhibited pH-responsive drug release and demonstrated significant tumor accumulation up to 24 hours post-injection. The targeted formulation significantly increased cell death in 4T1 cells at low concentrations while showing no cytotoxicity in CHO negative cells. In another study, Yi-Syun Shiao, *et al.* [43] designed a light-responsive nanoplatform based on AS1411-functionalized AuNPs for co-delivery of the photodynamic agent TMPyP4 and doxorubicin. Under 632 nm laser irradiation, the system simultaneously generated high levels of intracellular ROS and triggered controlled Dox release. In Dox-resistant MCF-7 cells, this combined approach produced significantly higher cytotoxicity compared to single-drug treatments, effectively overcoming multidrug resistance. The Au nanoparticle core provides inherent CT contrast capability for potential future imaging applications.

4.5. Study Limitations

Although this study provides proof-of-concept evidence for Au@GA NPs as dual radiosensitizers and CT CAs, several limitations should be acknowledged. Physicochemical characterization lacked FTIR, DLS, PDI, and zeta potential measurements, and colloidal stability in PBS or serum-containing medium was not evaluated, leaving Au@GA binding, hydrodynamic size, surface charge, and protein-corona effects incompletely defined. Cellular uptake and ROS generation were not directly quantified, and the mechanisms proposed for selective cytotoxicity and 6 MV radiosensitization therefore remain hypothesis-generating. The radiobiological assessment was limited to short-term MTT and Annexin V/PI assays in MCF-7/MCF-10A in vitro models, without clonogenic survival, multi-dose survival curves, or formal synergy modeling (Bliss independence or combination index), and only one 4 Gy fraction was tested; consequently, SER/DEF values could not be derived. CT attenuation was evaluated in phantoms rather than biological tissue, and no in vivo biodistribution, tumor accumulation, pharmacokinetics, or long-term toxicity data are available. Future studies should address these gaps

PROOF

through comprehensive physicochemical and stability characterization, intracellular gold and oxidative-stress assays, clonogenic multi-dose experiments with verified build-up/backscatter dosimetry, formal interaction modeling, tissue-mimicking or in vivo CT validation, and orthotopic BC models, ideally incorporating active targeting and immune-checkpoint combinations to advance translational potential.

5. Conclusion

In conclusion, this study successfully developed and characterized a green-synthesized, gallic acid-functionalized Au nanoparticle platform (Au@GA NPs) and systematically validated its dual theranostic capabilities for BC management, demonstrating that these NPs function as both potent radiosensitizers and superior CT CAs. Our findings establish that Au@GA NPs exhibit selective, concentration-dependent cytotoxicity towards MCF-7 BC cells (viability reduced to 68% at 200 μg/mL) while sparing normal MCF-10A epithelial cells (>82% viability), attributable to the intrinsic anticancer activity of GA and enhanced endocytic uptake in malignant cells. Furthermore, the NPs significantly potentiate radiation-induced cell death, reducing MCF-7 viability from 78% (radiation alone, 4 Gy) to 39% in combination treatment, representing a 50% absolute enhancement in radiosensitization efficacy, through synergistic physical mechanisms (photoelectric and Auger electron production due to Au's high atomic number, Z=79) and biological mechanisms (ROS generation and apoptotic pathway activation). The CT contrast evaluation revealed that Au@GA NPs provide up to 2.5-fold higher X-ray attenuation compared to the clinical agent Omnipaque at 80 kVp, positioning this platform as a superior imaging probe for precise tumor visualization and image-guided RT (IGRT). Flow cytometric analysis confirmed that the combination treatment synergistically induces apoptotic cell death (81.9% total non-viable cells, comprising 53.7% late and 27.5% early apoptosis) compared to radiation alone (25.7%), with minimal necrosis across all groups, indicating that cell death occurs through regulated pathways. Collectively, these results establish that Au@GA NPs represent a robust, cost-effective, and biocompatible theranostic platform that addresses the critical clinical challenges of RT resistance and inadequate imaging sensitivity in BC. While further in vivo validation, mechanistic elucidation, and optimization of treatment parameters are warranted, the simplicity and scalability of the green synthesis approach, combined with the intrinsic bioactivity of GA and superior physicochemical properties of the Au core, position Au@GA NPs as a highly promising candidate for personalized, image-guided RT applications. Future research directions should focus on comprehensive evaluation in orthotopic tumor models, exploration of combination strategies with immune checkpoint inhibitors to harness the abscopal effect, and investigation of targeting ligand conjugation to enhance active tumor homing, ultimately paving the way for clinical translation and improved outcomes for BC patients.

PROOF

Acknowledgments

The authors acknowledge the use of GapGPT (powered by OpenAI GPT-6) for generating the conceptual illustration used in the Graphical Abstract. All scientific representations, labels, and final visual layouts were reviewed, verified, and approved by the authors.

References

1- Joanne Kim *et al.*, "Global patterns and trends in breast cancer incidence and mortality across 185 countries." *Nature medicine,* Vol. 31 (No. 4), pp. 1154–62, (2025).

2- Xin Xiong *et al.*, "Breast cancer: pathogenesis and treatments." *Signal transduction and targeted therapy,* Vol. 10 (No. 1), p. 49, (2025).

3- K. Lu, Z. Sun, and Y. Yi, "Multidisciplinary strategies to reduce radiotherapy-induced cardiotoxicity in breast cancer: surgical and technological innovations." (in eng), *Front Oncol,* Vol. 15p. 1647080, (2025).

4- A. Zafar, S. Khatoon, M. J. Khan, J. Abu, and A. Naeem, "Advancements and limitations in traditional anti-cancer therapies: a comprehensive review of surgery, chemotherapy, radiation therapy, and hormonal therapy." (in eng), *Discov Oncol,* Vol. 16 (No. 1), p. 607, Apr 24 (2025).

5- M. G. Cerdas *et al.*, "Exploring the Evolution of Breast Cancer Imaging: A Review of Conventional and Emerging Modalities." (in eng), *Cureus,* Vol. 17 (No. 4), p. e82762, Apr (2025).

6- Hossein Omidian and Erma J Gill, "Multifunctional nanoplatforms bridging diagnostics and therapeutics in

cancer." *Micromachines,* Vol. 16 (No. 12), p. 1323, (2025).

7- Masoumeh Dastgir *et al.*, "Synergistic radiosensitization of breast cancer using bismuth oxide nanoparticles coated with chitosan and β-cyclodextrin loaded with curcumin and 5-aminolevulinic acid." *Cancer Nanotechnology,* Vol. 17 (No. 1), p. 8, (2026).

8- Giorgio Giuseppe Carbone *et al.*, "Exploring the potential of gold nanoparticles in proton therapy: mechanisms, advances, and clinical horizons." *Pharmaceutics,* Vol. 17 (No. 2), p. 176, (2025).

9- Reza Malekzadeh *et al.*, "Dose enhancement by gold, iron oxide, bismuth oxide, and platinum nanoparticles in radiotherapy: a comprehensive meta-analysis." *Radiological Physics and Technology,* Vol. 19 (No. 2), pp. 479–98, (2026).

10- Bahman Alipour *et al.*, "Advances in nano-scale metal-based contrast agents for computed tomography: a systematic review." *Radiation Physics and Chemistry,* Vol. 226p. 112195, (2025).

11- Nicolò Mauro, Mara Andrea Utzeri, Paola Varvarà, and Gennara Cavallaro, "Functionalization of metal and carbon nanoparticles with potential in cancer theranostics." *Molecules,* Vol. 26 (No. 11), p. 3085, (2021).

12- Omid Talaee *et al.*, "Characterization of a HER-2 targeted silica-gold nanoshells for breast cancer radio-photothermal therapy." *Applied Radiation and Isotopes,* p. 112454, (2026).

13- Sarkar Siddique and James CL Chow, "Application of nanomaterials in biomedical imaging and cancer therapy." *Nanomaterials,* Vol. 10 (No. 9), p. 1700, (2020).

14- Sanne M van de Looij, Erik R Hebels, Martina Viola, Mathew Hembury, Sabrina Oliveira, and Tina Vermonden, "Gold nanoclusters: imaging, therapy, and theranostic roles in biomedical applications." *Bioconjugate Chemistry,* Vol. 33 (No. 1), pp. 4–23, (2022).

15- Wilmmer Alexander Arcos Rosero, Angelica Bueno Barbezan, Carla Daruich de Souza, and Maria Elisa Chuery Martins Rostelato, "Review of advances in coating and functionalization of gold nanoparticles: from theory to biomedical application." *Pharmaceutics,* Vol. 16 (No. 2), p. 255, (2024).

16- Haniye Ahrabi, Reza Malekzadeh, and Ghazale Geraily, "Application of 5-aminolevulinic acid in cancer radio-dynamic therapy: A systematic review." *Radiation Physics and Chemistry,* Vol. 236p. 112910, (2025).

17- Hardeep S Tuli *et al.*, "Gallic acid: A dietary polyphenol that exhibits anti-neoplastic activities by modulating multiple oncogenic targets." *Anti-Cancer Agents in Medicinal Chemistry-Anti-Cancer Agents),* Vol. 22 (No. 3), pp. 499–514, (2022).

18- Seyed Mohammad Amini and Abolfazl Akbari, "Metal nanoparticles synthesis through natural phenolic acids." *IET nanobiotechnology,* Vol. 13 (No. 8), pp. 771–77, (2019).

19- Simona Tarantino *et al.*, "Revolutionizing radiotherapy: gold nanoparticles with polyphenol coating as novel enhancers in breast cancer cells—an in vitro study." *Discover Nano,* Vol. 20 (No. 1), p. 10, (2025).

20- José Antonio López Valverde, "Feasibility Evaluation of the Use of Gold Nanoparticles as Theragnostic Agents for Personalized and Precision Radiotherapy." *University of Seville*, (2024).

21- Xin Huang, Sarita Devi, Matteo Bordiga, Charles S Brennan, and Baojun Xu, "Phenolic compounds mediated biosynthesis of gold nanoparticles and evaluation of their bioactivities: A review." *International Journal of Food Science and Technology,* Vol. 58 (No. 4), pp. 1673–94, (2023).

22- Haniye Ahrabi *et al.*, "Dual-Purpose 5-Aminolevulinic Acid-Loaded iron oxide nanoparticles: enhancing radiotherapy and MRI in glioblastoma." *Journal of Drug Delivery Science and Technology,* p. 107853, (2025).

23- Xina Yu *et al.*, "Ellagic acid-enhanced biocompatibility and bioactivity in multilayer core-shell gold nanoparticles for ameliorating myocardial infarction injury." *Journal of nanobiotechnology,* Vol. 22 (No. 1), p. 554, (2024).

24- Hedieh Mansouri *et al.*, "A biocompatible theranostic nanoplatform based on magnetic gadolinium-chelated polycyclodextrin: in vitro and in vivo studies." *Carbohydrate polymers,* Vol. 254p. 117262, (2021).

25- Maedeh Yektamanesh, Yasin Ayyami, Marjan Ghorbani, Masoumeh Dastgir, Reza Malekzadeh, and Tohid Mortezazadeh, "Characterization of multifunctional β-cyclodextrin-coated Bi2O3 nanoparticles conjugated with curcumin for CT imaging-guided synergetic chemo-radiotherapy in breast cancer." *International Journal of Pharmaceutics,* Vol. 659p. 124264, (2024).

26- Yasin Ayyami *et al.*, "Characterization and application of targeted MnO2/CS@ ALA-MTX nano-radiosensitizers for boosting X-ray radiotherapy of brain tumors." *Colloids and Surfaces A: Physicochemical and Engineering Aspects,* Vol. 692p. 133975, (2024).

27- Saba Ziyaee, Reza Malekzadeh, Marjan Ghorbani, Behnam Nasiri Motlagh, Vahid Asghariazar, and Tohid Mortezazadeh, "Preparation of MnO2@ poly-(DMAEMA-co-IA)-conjugated methotrexate nano-complex for MRI and radiotherapy of breast cancer application." *Magnetic Resonance Materials in Physics, Biology and Medicine,* Vol. 36 (No. 5), pp. 779–95, (2023).

28- Bahman Alipour, Tohid Mortezazadeh, Waleed K Abdulsahib, Asghar Arzhang, Reza Malekzadeh, and Bagher Farhood, "A systematic review of multimodal application of quantum dots in breast cancer diagnosis:

PROOF

Effective parameters, status and future perspectives." *Journal of Drug Delivery Science and Technology,* Vol. 86p. 104682, (2023).

29- MJ Hernández-Esparza, Ilaria Fratoddi, Sara Cerra, K Juarez-Moreno, and R Huirache-Acuña, "Hybrid AuNPs-3MPS-MTX nanosystem and its evaluation for treating cervical cancer and melanoma." *Nanoscale Advances,* Vol. 5 (No. 24), pp. 7077–85, (2023).

30- M Rozalen, Manuel Sánchez-Polo, M Fernández-Perales, TJ Widmann, and José Rivera-Utrilla, "Synthesis of controlled-size silver nanoparticles for the administration of methotrexate drug and its activity in colon and lung cancer cells." *RSC advances,* Vol. 10 (No. 18), pp. 10646–60, (2020).

31- Priyanka Murawala, Amruta Tirmale, Anjali Shiras, and BLV Prasad, "In situ synthesized BSA capped gold nanoparticles: effective carrier of anticancer drug methotrexate to MCF-7 breast cancer cells." *Materials Science and Engineering: C,* Vol. 34pp. 158–67, (2014).

32- Behnaz Babaye Abdollahi, Marjan Ghorbani, Hamed Hamishehkar, Reza Malekzadeh, and Alireza Farajollahi, "Synthesis and characterization of actively HER-2 Targeted Fe3O4@ Au nanoparticles for molecular radiosensitization of breast cancer." *BioImpacts: BI,* Vol. 13 (No. 1), p. 17, (2022).

33- Behnaz Babaye Abdollahi *et al.*, "Main approaches to enhance radiosensitization in cancer cells by nanoparticles: A systematic review." *Advanced pharmaceutical bulletin,* Vol. 11 (No. 2), p. 212, (2020).

34- Devika B Chithrani *et al.*, "Gold nanoparticles as radiation sensitizers in cancer therapy." *Radiation research,* Vol. 173 (No. 6), pp. 719–28, (2010).

35- Somayeh Sadat Mehrnia, Bijan Hashemi, Seyed Javad Mowla, Maryam Nikkhah, and Azim Arbabi, "Radiosensitization of breast cancer cells using AS1411 aptamer-conjugated gold nanoparticles." *Radiation Oncology,* Vol. 16 (No. 1), p. 33, (2021).

36- Fatemeh Ghahremani, Daryoush Shahbazi-Gahrouei, Amirhosein Kefayat, Hasan Motaghi, Masoud A Mehrgardi, and Shaghayegh Haghjooy Javanmard, "AS1411 aptamer conjugated gold nanoclusters as a targeted radiosensitizer for megavoltage radiation therapy of 4T1 breast cancer cells." *RSC advances,* Vol. 8 (No. 8), pp. 4249–58, (2018).

37- Emad khoshdel *et al.*, "Gold nanostructure-based cancer photothermal therapy: a comprehensive systematic review, meta-analysis, and dose–response evaluation." *Cancer Nanotechnology,* (2026).

38- Reza Malekzadeh *et al.*, "Nanoarchitecture-based photothermal ablation of cancer: a systematic review." *Environmental Research,* Vol. 236p. 116526, (2023).

39- Mohammadreza Ghaffarlou *et al.*, "Photothermal and radiotherapy with alginate-coated gold nanoparticles for breast cancer treatment." *Scientific reports,* Vol. 14 (No. 1), p. 13299, (2024).

40- Sepideh Hassibian *et al.*, "Surface modification of hollow gold nanoparticles conducted by incorporating cancer cell membrane and AS1411 aptamer, aiming to achieve a dual-targeted therapy for colorectal cancer." *International Journal of Pharmaceutics,* Vol. 655p. 124036, 2024/04/25/ (2024).

41- Cheng-Hung Li *et al.*, "Fluorescence-guided probes of aptamer-targeted gold nanoparticles with computed tomography imaging accesses for in vivo tumor resection." *Scientific reports,* Vol. 5 (No. 1), p. 15675, (2015).

42- Sahar Taghavi *et al.*, "Surface engineering of hollow gold nanoparticle with mesenchymal stem cell membrane and MUC-1 aptamer for targeted theranostic application against metastatic breast cancer." *European Journal of Pharmaceutics and Biopharmaceutics,* Vol. 187pp. 76–86, (2023).

43- Yi-Syun Shiao, Huai-Hsuan Chiu, Pin-Hsuan Wu, and Yu-Fen Huang, "Aptamer-functionalized gold nanoparticles as photoresponsive nanoplatform for co-drug delivery." *ACS applied materials & interfaces,* Vol. 6 (No. 24), pp. 21832–41, (2014).

PROOF